Stress relaxation of nickel-based superalloy helical springs at high temperatures

Simon P.A. Gill[1*], Gordon McColvin[2], Andrew Strang[1]

[1] Department of Engineering, University of Leicester, University Road, Leicester, LE1 7RH

[2] Alstom Power Ltd, Newbold Road, Rugby, CV21 2NH

* corresponding author (spg3@le.ac.uk)

Abstract.

The creep resistance of materials in spring applications is generally acknowledged to be well below that observed in other applications. Helical springs formed from three candidate nickel-based superalloys, Nimonic 90, René 41 and Haynes 282, have been tested under compression in order to gain some insight into this phenomenon. Stress relaxation tests conducted at 600-700°C found that, under constant displacement, the degradation of the spring force is one to three orders of magnitude faster than would be predicted from creep data from extruded samples under equivalent tensile loading. An analytical model for torsional creep in helical springs is derived from a modified version of the Dyson creep model. The effects of various microstructural features on the deformation rate are considered. Effects such as the coarsening of the precipitate-strengthening gamma-prime phase, tertiary creep due to dislocation multiplication, damage evolution and hardening due to transfer of the stress to the particles from the matrix are concluded to make negligible contributions. It is predicted that the poor performance of the springs is due to the very high population of geometrically necessary dislocations that result from the bending and twisting of the wire into a helical coil. It is expected that these dislocations are resistant to conventional heat treatments, resulting in a persistent residual stress field and a large number of dislocations to facilitate the creep process. In some cases, the stress relaxation is found to be so fast that the precipitate hardening of the alloy is too slow to prevent significant initial degradation of the spring.

Keywords : Stress relaxation, torsional creep, geometrically necessary dislocations, helical springs;

1. Introduction

Metallic wire, helical coil compression springs continue to be of considerable practical interest in many high temperature plant applications, but to date have failed to live up to expectations based upon axial creep properties. Springs of this type are used extensively in power plant surface clearance control systems. The inspiration to delve further into the issues of springs for high temperature service arises from a potential requirement for spring materials to match the needs of ever increasing power plant temperatures. This will enable increased operating temperatures and reduced CO_2 emissions per Megawatt.

A mechanical modelling approach has been adopted to highlight those materials and engineering characteristics that would best lead to a wire wound helical coil compression spring that will operate at higher temperatures more in keeping with the known high temperature properties of the parent material. The modelling approach has been matched with practical investigation of coil springs in three common usage nickel-based superalloys well known for their high temperature creep strength: Nimonic 90, René 41 and Haynes 282. The materials selected are available as fine wire product and all exhibit good fabricability in coil forming.

Nimonic 90 was developed as an age-hardenable creep resistant alloy for temperatures up to about 920°C. It has good ductility and is typically used in turbine blades, ring sections, hot working tools, forgings and high temperature springs [15]. René 41 was designed to be used in high stress applications within the 650-980°C temperature range. René-41 is difficult to fabricate due to its higher gamma-prime fraction and it also work hardens rapidly, requiring frequent annealing stages. As a material with good resistance to oxidation and corrosion, it is often used in applications such as after-burner components, turbine casings and fasteners [16], however it is known to suffer from strain age cracking. Haynes-282 is a more recent alloy developed as a successor to Waspaloy and René-41. It combines good thermal stability, weldability, and fabricability not found in many commercial alloys, and has excellent creep strength equal to that of René-41, in the temperature range of 649-927°C. Slow gamma-prime precipitation kinetics result in excellent ductility in the as-annealed state. It is often used in components in critical areas of gas turbines, combustors, compressors and exhaust/nozzle applications [17].

The experimental procedure for measuring the stress relaxation in the springs is outlined in section 2. A simple, analytical model for this stress relaxation is developed in section3. Section 4 compares the predictions of the model with the experimental results and proposes explanations for the lower than expected performance of nickel-based superalloy springs and how it can be improved.

2. Materials and experimental procedure

The primary objective of the study was to determine the compressive stress relaxation behaviour of close wound helical springs suitable for operation at temperatures in the range 600°C to 750°C. Accordingly three creep resistant nickel-base alloys, Nimonic 90, Rene 41 and Haynes Alloy 282, were selected as potential candidates for applications within this temperature range. In each case the alloys were supplied to spring manufacturers as solution treated 30% cold drawn to 2.5 mm diameter wire, i.e. in the "spring tempered condition", as is normal for wire coil spring manufacture. The springs were then cold wound to the required dimension on a mandrel and subsequently given a precipitation hardening treatment appropriate to each alloy. The Nimonic 90 springs were manufactured by Alstom Power and the René 41 and Haynes 282 springs were manufactured by European Springs and Pressings Ltd. Details of the nominal compositions of the alloys are shown in Table 1.

Wt%	Ni	Cr	Co	Mo	Ti	Al	Fe	Mn	Si	C	B
H282	57.7	19.57	10.23	8.5	2.1	1.43	0.37	0.02	0.05	0.061	0.006
N90	53	19.5	18	N/A	2.4	1.4	3	1	1.5	0.13	N/A
R41	52.5	19	11.06	9.67	3.11	1.56	2.93	0.07	0.05	0.08	0.006

Table 1 : nominal compositions in wt% of the three nickel-based superalloys in the experimental trial : Nimonic 90 (N90), René 41 (R41) and Haynes 282 (H282).

The solution treatment and post spring winding heat treatments for the three alloys are given in Table 2. Note that Haynes 282 is the only alloy that undergoes a two stage precipitation hardening heat treatment. The René 41 requires the highest precipitation hardening conditions to achieve the optimum precipitate distribution for high temperature strength and ductility, as it has the highest concentration of gamma-prime forming elements.

Alloy	Wire solution treatment temperatures (^{o}C)	Spring precipitation treatment temperatures (^{o}C)
Haynes 282	1150°C rapid cool	2 hrs 1010°C AC+ 8 hrs 788°C AC
Nimonic 90	1150°C rapid cool	4 hrs 750°C AC
René 41	1080°C rapid cool	16 hrs 760°C AC

Table 2: Solution and final precipitation heat treatments for the superalloy wire and helical springs (AC = air cooled).

In the present studies the helical springs wound from 2.5mm diameter wire were 29mm in height with outside and inside diameters of 19mm and 14mm respectively, as shown in Figure 1. Each spring consisted of five free coils and two end coils which were tapered and flattened. Following measurement of the overall free length of each of the springs, they were fully compression tested in an Instron Tensometer to determine their load /displacement characteristics, as shown in Figure 2. This enabled the spring constant for each candidate material to be determined as well as the load required for any predetermined compression of each spring. No significant difference between the spring constants for the three alloys was observed.

Figure 1: The spring in the bolt assembly. The ends of the springs are flattened and tapered. The spring is subjected to a fixed compressive displacement δ using a tightened nut and bolt.
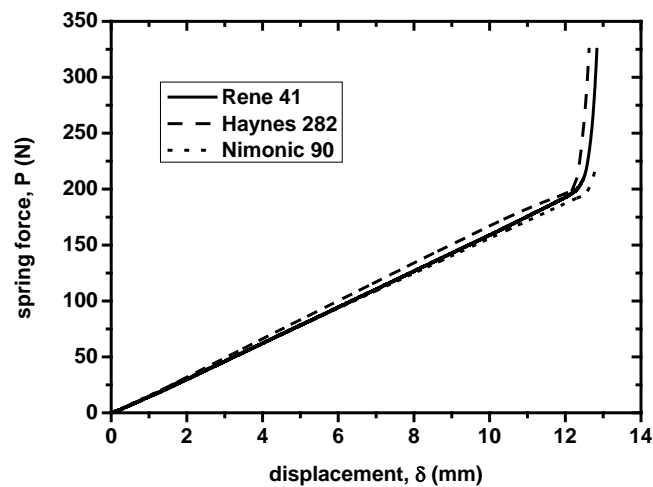

Figure 2: Compressive load-displacement plots for the springs in the as-supplied condition

The compressive stress relaxation tests were conducted on helical springs using the procedure described by Betteridge [22]. In order to determine the effects of long-term thermal exposure on the compressive stress relaxation of the springs, samples of each alloy were placed on a 12mm diameter stainless steel bolt with washers at each end and pre-compressed to lengths of 19mm, 21mm and 23 mm, as shown in Figure 1. Nuts were screwed down to lock the displacements and the loads corresponding to each displacement condition recorded. The bolted assemblies for each of the three alloys and three compressive displacements were then placed in furnaces set at 600°C, 650°C and 700°C for exposure durations of 1, 3, 10, 30, 100, 300 and 1000 hours. Three springs were used for

4

every test and the remnant force reported for each test is the average over the three results. In every case the standard deviation was very small, indicating that the results were very reproducible.

Following each period of exposure batches of samples were removed from the furnaces and allowed to cool to room temperature. The assemblies were then disassembled and the overall length of each spring recorded. This was followed by compression displacement tests on each of the exposed samples which allowed the residual force in the spring and the spring constant to be determined, as shown in Figure 3. The ratio of the load supplied by the thermally exposed spring relative to that in the original as-supplied spring is used to indicate the degree of load relaxation that occurred during the test. Data for each alloy for the three initial spring compression conditions can then be plotted as diagrams of load relaxation against exposure time up to 1000hrs for each of the tests at 600°C, 650°C and 700°C. This is presented in section 4.1 alongside the model predictions. The spring constant was not found to be significantly affected by the stress relaxation process. Also, it was found that the distance between the free coils always stays a fixed proportial of the distance between the ends of the spring during the stress relaxation tests. This implies that the ends of the springs behave in a similar fashion to the rest of the spring. This is an important observation for the next section, where a model is developed for predicting the stress relaxation response in the free coils of the spring such that end effects are neglected.
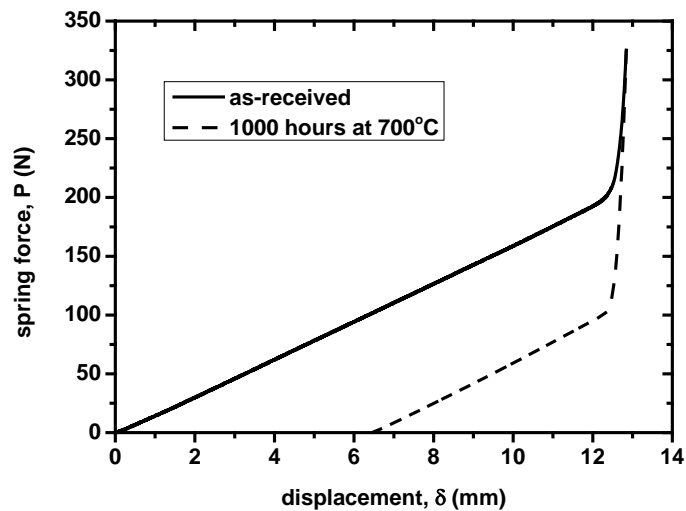
Figure 3: Comparison of the load-displacement response for an as-received Haynes 282 spring and a similar spring following 1000hrs exposure at 700 °C under a fixed 10mm compressive displacement.

3. Modelling the stress relaxation of springs

This section develops and explores theoretical models that can explain the observed experimental data. Firstly the initial stresses in the deformed linear, elastic spring are established in section 3.1. The creep model for the nickel-based superalloys under study is introduced in section 3.2. These two models are then combined in section 3.3 to develop a simplified, analytic model for the stress relaxation in a cylindrical wire under torsion. Full finite element modelling of the stress relaxation in a helical spring is undertaken in section 3.4 for comparison. The effect of further physical processes is considered in sections 3.5 and 3.6. Firstly the development of a back stress is included due to partial transfer of the load from the matrix to the particulate phase. Tertiary creep in the context of dislocation multiplication is also considered in section 3.5. Section 3.6 looks at the evolution of the gamma prime particles in these precipitate strengthened materials, namely particle coarsening and further post-heat treatment precipitation of gamma prime. Finally a summary of the final model is given in section 3.7.

3.1 Stresses in the spring

Neglecting the small contribution from the pitch of the spring, the length of wire in a spring of coil radius R consisting of N coils is $L = 2\pi RN$, where R is defined to be the average of the minimum (inside) and maximum (outside) coil radii. If the spring is vertically compressed a distance δ then the total torsional rotation of the wire due to this downward movement is δ/R. The rotation per unit length (twist) is therefore

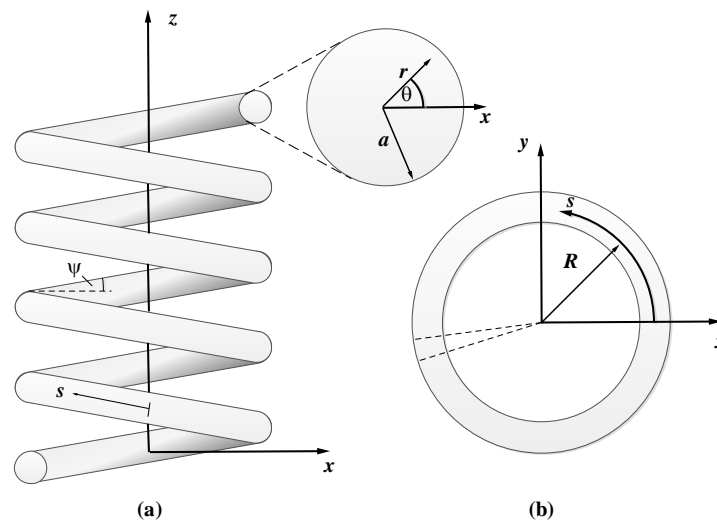$$\phi = \frac{\delta}{2\pi R^2 N}.$$
(3.1)

Figure 4: The spring geometry. (a) Side view showing the distance travelled along the length of the wire, s, and the pitch angle ψ. The exploded view of the wire section shows the distance from the centre of the wire, r, at an angle θ to the xy-plane. The base of the spring is in the xy-plane and z is the helical axis. (b) Plan view showing the mean radius of the coil R. The dashed lines indicate a small wire segment.

Initially we neglect the contribution from the shear force acting on the wire, as well as the effect of the curvature (R) and pitch (ψ). This essentially assumes that the response of the helical spring is equivalent to that of a straight, cylindrical wire of radius a, subject to a pure torsion of ϕ per unit length. In this case, the only stress in the wire is the torsional shear stress

$$\gamma_{\theta s}(r) = r\phi \tag{3.2}$$

where r is the radial distance from the central longitudinal s-axis running along the wire length and θ is the angle between r and the horizontal xy plane, as shown in Figure 4. The torque per unit length required to achieve this twisting is

$$Q_0 = \int_0^{2\pi} \int_0^a r^2 \tau_{\theta s} dr\, d\theta = 2\pi G\phi \int_0^a r^3 dr = \frac{\pi G\phi a^4}{2} \tag{3.3}$$

where the shear stress $\tau_{\theta s} = G\gamma_{\theta s}$ and G is the shear modulus. Given that the torque applied to the spring by a vertical compressive force P_0 is $Q_0 = P_0 R$, the linear elastic force-displacement relation for the straight wire spring approximation is therefore

$$P_0 = k\delta \tag{3.4}$$

where the spring (stiffness) constant

$$k = \frac{Ga^4}{4R^3 N}. \tag{3.5}$$

For the given geometry of a=1.25mm and R=8.25mm, it is found that the spring constant of the springs both before and after testing (there is little significant change) is 17.5N/mm. Given a room temperature shear modulus of G_0=82.5GPa this equates to a spring with N=5.12 effective coils. The true number of "complete" coils in the spring is not clearly defined, as the ends of the spring wire are tapered and flattened.

The simple model for a straight cylindrical wire suggests that the maximum shear strain due to torsion is $\gamma_{\theta s}^{max} = a\phi$. For the curved wire, with average radius of curvature R, the variation in the width of a curved arc segment, as indicated by the dashed lines in Figure 4b, relative to the mean width is $1 + \left(\frac{r}{R}\right)\cos\theta$. A simple model for the strain variation through the cross-section that takes into account the curvature of the wire is therefore

$$\gamma_{\theta s}(r, \theta) = \frac{r\phi}{1 + \left(\frac{r}{R}\right)\cos\theta}. \tag{3.6}$$

This first order correction to the model for wire curvature shows that the shear strain at the innermost point of the spring wire $\gamma_{\theta s}^{max} = \frac{c}{c-1} a\phi$ is now the maximum shear strain, where $c = \frac{R}{a}$ is known as the spring index and $\frac{c}{c-1}$ is known as the stress correction factor [8]. Higher order corrections to the stress correction factor have been proposed and investigated [8]. In this paper we have c=6.6 which suggests that to first order there is a stress correction factor of 1.179. This compares favourably with results from finite element calculations which find 1.213 [8]. If the pitch of the spring, $\psi = \sin^{-1}(h/L)$, is included then the radius of curvature of the coils increases slightly

from R to $R/cos\psi$. Here we have h=29mm so the pitch correction factor $1/cos\psi$ is 1.006. The effect of this adjustment is negligible. Therefore, to first order, we expect the stresses in a zero-pitch (toroidal) wire under torsion to be very similar to those in the helical spring. This concurs with the results of finite element calculations for small pitches [8]. To first order, the torque induced in the wire is now written as

$$Q_0 = G \int_0^{2\pi} \int_0^a r^2 \gamma_{\theta s} \left(1 + \left(\frac{r}{R}\right) cos\theta\right) dr \, d\theta = \frac{\pi G \phi a^4}{2} \qquad (3.7)$$

This is identical to **(3.3)** demonstrating that although the stress distribution in a straight wire is different than in a helical spring [11], the net effect on the linear elastic response of the spring is a second order effect in c.

As well as the torsional shear stress, $\tau_{\theta s}$, there is also a shear stress $\tau_{zs} = P_0/A_z$ to balance the applied shear force P_0, where $A_z = \pi a^2/cos\psi$ is the resolved cross-sectional area of the wire in the z-direction. As we have seen above, the pitch effect is negligible such that the effective shear stress at a point is $\tau = \sqrt{\tau_{\theta s}^2 + \tau_{zs}^2}$. We have $\left(\frac{\tau_{zs}^{max}}{\tau_{\theta s}^{max}}\right)^2 = \frac{1}{4c^2}$=0.005 and therefore it is found that 99.5% of the load carried by a spring with c=6.6 is due to torsion of the wire and hence in a simple analytical model the contribution from the shear force can be neglected. Consequently we simply write $\gamma = \gamma_{\theta s}$ and $\tau = \tau_{\theta s}$ for the subsequent duration of the paper. This is why **(3.4)** and **(3.5)** have been widely and effectively used in the analysis of springs, although they strictly apply to a straight wire under pure torsion.

For comparison with standard uniaxial tensile creep tests we consider the effective strain $\epsilon_e = \gamma/\sqrt{3}$ and the effective (von Mises) stress $\sigma_e = \sqrt{3}\tau$ in the spring [3]. The applied end displacements used here are δ=6, 8 and 10 mm. These equate to maximum effective strains of ϵ_e^{max} =0.34%, 0.45% and 0.57% for a straight wire and ϵ_e^{max} =0.41%, 0.54% and 0.68% for a curved spring. To determine the maximum effective stresses it is important to take the effect of temperature on the modulus into account. We use a standard approximation that the modulus halves as the melting temperature is approached, $G(T) = G_0(1 - \frac{T-300}{2(T_m-300)})$, where T_m=1643K. This is a reasonable fit to the experimental data over the temperature range of interest [15]. Therefore σ_e^{max}=382MPa, 511MPa and 638MPa at 600°C for a straight wire and σ_e^{max}=449 MPa, 602 MPa and 752MPa for a curved spring. Although the applied load on the springs is small, P_0=105-175N, the stresses are very large. For reference, the 0.1% proof stress for Nimonic 90 at 600°C is approximately 700MPa [5] and the tensile strength is 1040MPa [4]. This suggests that some initial plastic yielding should occur in a very small area around the innermost section of the spring wire at 600°C at the highest applied displacement of 10mm although there is no evidence for this. This is thought to be due to residual stresses in the wire (see section 4.3). The inelastic response of the spring materials is now investigated in the context of uniaxial tensile creep.

3.2 The Dyson creep model
The physics-based creep law of Dyson [5] is adopted to model the time-dependent relaxation of the stresses in the springs. This has been widely applied to high gamma-prime fraction nickel-based superalloys such as CMSX-4 [10], as well as medium gamma-prime fraction superalloys such as Nimonic 90 [5]. One of the advantages of this model is that it is derived from physical principles, so

the material constants are related to measurable material properties. The physical model assumes dislocation climb as the dominant mechanism. Harrison et al [4] show in a physics-based deformation map that dislocation climb is expected to be an important creep mechanism for effective stresses in the range of 80-640 MPa for Nimonic 90. At high stresses particle shearing becomes more important and dominates above 640MPa. At lower stresses diffusion creep is more active and below 80MPa it is expected to be the dominant mechanism. Atkinson and Gill [9] have extended the Dyson creep model to include particle shearing (high volume fraction superalloys) and strengthening of the matrix (low volume fraction superalloys), although incorporation of either effect is not expected to be necessary for the medium volume fraction superalloys considered here. The uniaxial creep strain rate in this case is derived to be the following function of the applied stress σ

$$\frac{d\epsilon^c}{dt} = A\sinh(\alpha\sigma). \tag{3.8}$$

where the two material parameters

$$A = \rho(1 + \eta)(1 - f)D_s/M. \tag{3.9}$$

and

$$\alpha = \frac{b^2 \eta r_p}{M k_B T}(1 - H) \tag{3.10}$$

are defined in terms of the dislocation density ρ, the gamma-prime volume fraction f, the diffusion coefficient, $D_s = 10^{-4} \exp(-\frac{3.2x10^5}{R_G T})$, the burger's vector b=0.25nm, the particle spacing-to-radius ratio, $\eta = 1.6\left(\sqrt{\frac{\pi}{4f}} - 1\right)$ and the particle radius, r_p, where k_B is Boltzmann's constant, R_G is the gas constant, T is temperature in Kelvin, M=3 is Taylor's constant for a polycrystalline material and H is a hardening parameter which models the development of a back stress and the transition from primary to secondary creep. Note that Dyson proposes a slightly different pre-factor $A = \rho\eta f(1 - f)D_s/M$. Equation **(3.9)** is a modified expression proposed by Atkinson and Gill [9] which takes into account glide in addition to climb and was found to more closely fit the creep data presented in this paper. The accumulation of damage is not represented in **(3.8)**. This is reasonable as the total plastic strains (<1%) here are too small for this to be a necessary consideration. Dyson [5] proposes the following expression for the equilibrium volume fraction as a function of temperature

$$f(T) = \frac{c_0 - c_E(T)}{0.23 - c_E(T)} \tag{3.11}$$

where c_0 is the combined mol% concentration of gamma-prime forming elements (Al and Ti for the alloys considered here) and $c_E = 17\exp\left(-\frac{7250}{T}\right)$ is their combined equilibrium matrix concentration. In general the volume fraction increases with c_0 and decreases with temperature.

Mustata et al. [12] express **(3.8)** for a multiaxial stress state σ_{ij} as

$$\frac{d\epsilon_{ij}^c}{dt} = \frac{3s_{ij}}{2\sigma_e} A\sinh(\alpha\sigma_e). \tag{3.12}$$

where the deviatoric stress, $s_{ij} = \sigma_{ij} - \frac{1}{3}\sigma_{kk}\delta_{ij}$, determines the creep direction and the von Mises effective stress, $\sigma_e = \sqrt{\frac{3s_{ij}s_{ij}}{2}}$, determines the creep rate.

The evolution of the back stress during primary creep, $\sigma_b = H\sigma_e$, is given by [5]

$$\frac{d\sigma_b}{dt} = \frac{Ef}{(1-f)}\left(1 - \frac{\sigma_b}{\sigma_b^*}\right)\frac{d\epsilon_e^c}{dt}. \tag{3.13}$$

where the effective creep strain $\epsilon_e^c = \sqrt{\frac{2\epsilon_{ij}^c\epsilon_{ij}^c}{3}}$ and the maximum back stress $\sigma_b^* = H^*\sigma_e$ with $H^* = \frac{2f}{1+2f}$. Tertiary creep is incorporated into the model via dislocation multiplication such that

$$\frac{d\rho}{dt} = \rho_0 K_0 \frac{d\epsilon_e^c}{dt} \tag{3.14}$$

where ρ_0 is the initial dislocation density and $K_0 = 300$ [5] is a multiplication constant.

The calibration for this model is shown for Nimonic 90 in Figure 5 against data for an extruded section subsequently cold rolled [15]. The fit is extremely good at predicting the applied stresses required to generate creep strains of 0.1% and 0.2% at given times, and is reasonable for 0.5%, although the stress required is slightly overestimated, i.e. the stress-dependence is underestimated. Similar calibrations were conducted for René 41 [16] and Haynes 282 [17] from available creep data. The material input parameters are given in Table 3. As discussed in section 1, the manufacturers quoted creep performance of Haynes 282 and René 41 extruded sections in the chosen temperature range are comparable and marginally better than that of Nimonic 90. The creep model outlined here for uniaxial tensile loading is now developed for the case of torsional stress relaxation in the spring wire.
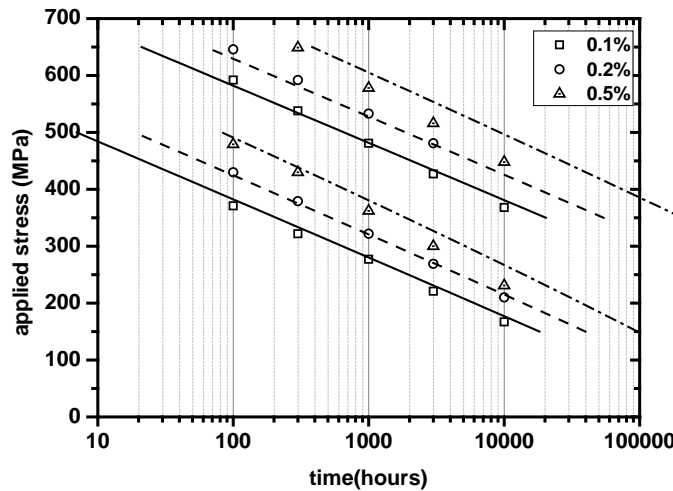
Figure 5 : The calibration of the uniaxial creep model for Nimonic 90 at 600°C (upper curves) and 700°C (lower curves) using creep stress data for accumulated plastic strains of 0.1%, 0.2% and 0.5% for an extruded section subsequently cold rolled [15].

Alloy	Particle radius, r_p	Dislocation density, ρ_0	Concentration, c_0
Nimonic 90	10 nm	0.3×10^{10} m^{-2}	5.7 mol%
René 41	10 nm	10^{10} m^{-2}	7.0 mol%
Haynes 282	7.5 nm	10^{10} m^{-2}	5.7 mol%

Table 3 : Material parameters for the variant Dyson creep model (3.8) calibrated from uniaxial tensile creep tests on extruded sections.

3.3 An analytical solution for stress relaxation in a straight, cylindrical wire under pure torsion due to steady state creep

For a purely torsional stress state (3.2), (3.12) can be used to express the local shear creep strain γ^c in terms of the local shear stress τ as

$$\frac{d\gamma^c}{dt} = \sqrt{3}A sinh(\sqrt{3}\alpha\tau). \tag{3.15}$$

This is similar in form to the uniaxial case (3.8) with M replaced by $M/\sqrt{3}$. The instantaneous shear stress arises from the elastic shear strain, $\tau = G\gamma^e$, where the total shear strain $\gamma = \gamma^e + \gamma^c$ is the sum of the elastic shear strain and the creep shear strain [1]. From (3.6) we write $\gamma^c = gr\phi$, where $g(r,\theta) = \left(1 + \left(\frac{r}{R}\right)cos\theta\right)^{-1}$. Hence

$$\frac{d\gamma^c}{dt} = \sqrt{3}A sinh(\sqrt{3}\alpha G(gr\phi - \gamma^c)). \tag{3.16}$$

To make analytical progress, we now make some simplifying assumptions about the constitutive law. These will be validated against the full model in sections 3.4 and 3.5. Firstly, steady state primary creep is assumed by neglecting the back stress ($H = 0$) and dislocation multiplication ($\rho = \rho_0$). As the initial creep rate is typically the fastest (for plastic strains <1%) this assumption is expected to slightly overestimate the creep rate. As the stress relaxation of the spring is controlled for the majority of the process by the highly stressed regions near the outside of the wire (large r) we make the additional assumption that $sinh(x) \approx \frac{1}{2}(e^x - 1)$ for $x \gg 1$, where the one is included to give the correct asymptotics as $x \rightarrow 0$. Therefore (3.16) is approximated as

$$\frac{d\gamma^c}{dt} = \frac{1}{2}A_0 \left[\exp(\beta(gr\phi - \gamma^c)) - 1\right]. \tag{3.17}$$

where $A_0 = \sqrt{3}\rho_o(1 + \eta)(1 - f)D_s/M$ and $\beta = \frac{\sqrt{3}Gb^2\eta r_p}{Mk_BT}$ are constants. This can be integrated over time such that

$$\gamma^c(r,t) = gr\phi + \frac{1}{\beta}\ln\left[1 - \exp\left(-\frac{1}{2}A_0\beta t\right)(1 - \exp(-\beta gr\phi))\right] \qquad (3.18)$$

The torque applied to the spring to maintain the torsion ϕ is derived from **(3.7)**

$$Q(t) = P(t)R = G\int_0^{2\pi}\int_0^a r^2(gr\phi - \gamma^c)\left(1 + \left(\frac{r}{R}\right)\cos\theta\right)dr\,d\theta \qquad (3.19)$$

and therefore the relative force in the spring (compared to its initial value) is

$$\frac{P(t)}{P_0} = -\frac{2}{\beta\pi\phi a^4}\int_0^{2\pi}\int_0^a \frac{r^2}{g}\ln\left[1 - e^{-\frac{1}{2}A_0\beta t}(1 - e^{-\beta g r \phi})\right]dr\,d\theta. \qquad (3.20)$$

Numerical calculations show that the inclusion of g has negligible effect (some terms cancel due to symmetry and others are small) such that it is reasonable to assume $g = 1$. The integrals can then be evaluated analytically to give

$$\frac{P(t)}{P_0} = -\frac{4}{3h}\left[\ln(1-y) + \sum_{n=0}^{2}\frac{6}{n!\,h^{3-n}}S\left(4 - n, \frac{ye^{-h}}{y-1}\right) - \frac{6}{h^3}S\left(4, \frac{y}{y-1}\right)\right] \qquad (3.21)$$

where $h = \beta a\phi$ is a dimensionless group, $y = \exp\left(-\frac{1}{2}A_0\beta t\right)$ is the measure of time and $S(m,z) = \sum_{p=1}^{\infty}\frac{z^p}{p^m}$ is the polylogarithmic function. Even further simplification can provide more insight into what controls the creep process. If we assume that $e^{-\beta r\phi} \ll 1$ then **(3.20)** is easily evaluated as

$$\frac{P(t)}{P_0} \approx -\frac{4}{3h}\ln(1-y) \qquad (3.22)$$

which is equivalent to ignoring the last two terms in **(3.21)**. Note that this expression does not have the correct asymptotics as $t \to 0$, and hence this expression is not expected to be valid at early times. In addition, at later times $e^{-\beta r\phi} \ll 1$ is not valid, so it is expected that **(3.22)** only applies for roughly $0.3 < \frac{P}{P_o} < 0.7$. In this regime it is expected that $A_0\beta t \ll 1$ so a further simplification is

$$\frac{P(t)}{P_0} \approx -\frac{4}{3h}\left[\ln(t) + \ln\left(\frac{1}{2}A_0\beta\right)\right]. \qquad (3.23)$$

This is a useful expression as it implies that a plot of P/P_0 against $\ln(t)$ will yield a linear fit (in the region of validity) where the creep exponent β can be determined from the slope and the creep pre-factor A_o can be determined from the intercept.

These expressions are fitted to the results for a single stress relaxation test on a Nimonic 90 spring at 600°C in Figure 6. The force vs time plot in Figure 6a shows that the model using the uniaxial creep data ($\rho_0 = 0.3x10^{10}m^{-2}$) is clearly very poor. However, a good fit is obtained in this case (in the absence of the hardening factor H) for $\rho_0 = 10^{12}$. This is simply equivalent to rescaling the time axis, but indicates that the stress relaxation in the spring is roughly 300 times faster than would be expected in an extruded bar in tension. For the remaining duration of this paper, only force vs $\log_{10}(t)$ plots will be presented, such as that shown in Figure 6b. This more clearly shows the short

term and long term asymptotics of the behaviour. It also demonstrates the predicted linear regime in the middle of the profile for $0.3 < \frac{P}{P_o} < 0.7$ and shows the limits of the simple expressions **(3.22)** and **(3.23)**, which are identical for $\frac{P}{P_0} > 0.2$. The predictions from this simple analytic model are now compared with the exact solution obtained from finite element simulations.
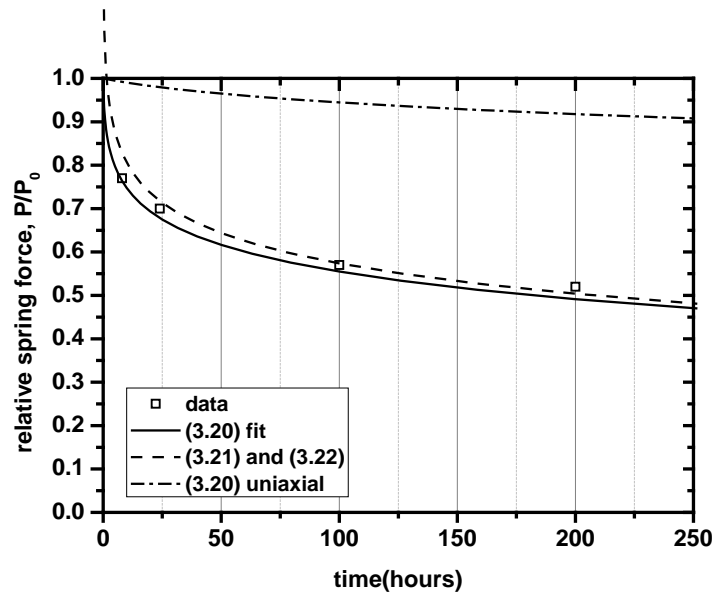
(a)
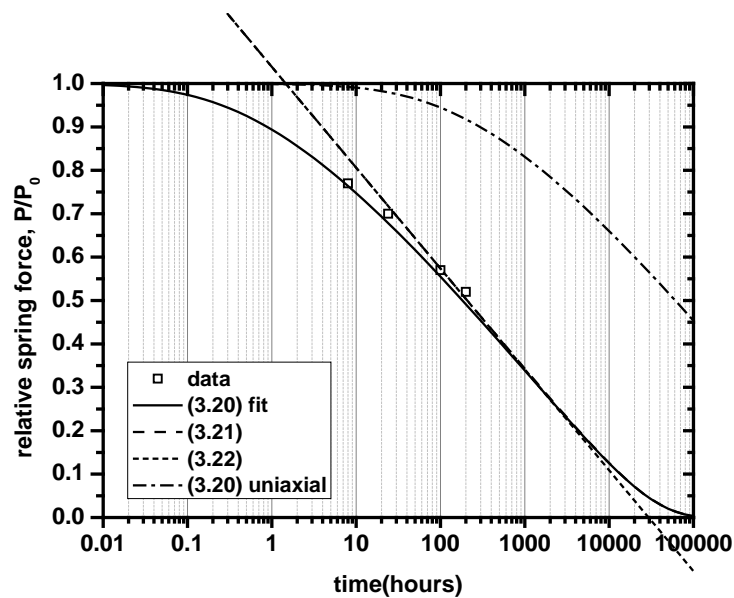
(b)

Figure 6 : Comparison of the analytical stress relaxation models **(3.21)**, **(3.22)** and **(3.23)** against experimental data for Nimonic 90 at 600°C with δ=9mm for (a) time t, and (b) $\log_{10}(t)$ on the horizontal axis.

3.4 Comparison between stress relaxation due to steady state creep in a straight wire, a zero-pitch spring and a helical spring by finite element analysis

In the derivation of the analytical model **(3.21)** it has been assumed that the spring wire is subjected to a purely torsional stress state **(3.2)**, with the conclusion that the first order correction **(3.6)** has no net elastic effect, and that higher order corrections are small. In addition, the shear stress τ_{rs} has also been ignored as small. In this section, the general form of the creep law **(3.12)** is employed in finite element calculations with the same steady state creep rate assumptions of section 3.3. Firstly pure torsional creep in a straight cylindrical wire was simulated. The stress relaxation of the wire was found to be identical to the predictions of the analytical model **(3.21)** as required. The effect of the wire curvature R was evaluated by simulating a 2% length of a single helical coil (a 7.2^0) section, as shown in Figure 7. Both end faces were displaced in the z-direction (the direction of compression) by a distance $w = \frac{\delta}{2} * (\frac{0.02}{5.15})$ at the centre point of each face, one upwards and one downwards. This induces the initial torsional rotation per unit length ϕ and the corresponding torque Q_0 and the shear force P_0. The end faces must also be rigidly rotated by an amount w/l around the radial tangent to each end face to avoid inducing bending in the segment, where $l = 0.02 * 2\pi R$ is the length of the segment. The faces were allowed to move radially outwards. The effect of varying the pitch angle ψ was evaluated. The calculations were conducted in COMSOL Multiphysics v4.3 using the non-linear materials module with the Garofalo (hyperbolic sine) creep model. The stress relaxation response of a straight wire **(3.21)**, a zero-pitch (toroidal) wire and the actual helical spring geometry was determined[20]. They are not illustrated here, as all the geometries gave almost identical, visually indistinguishable results. Given the negligible discrepancy between the different approaches, it is therefore proposed that for the rest of the paper the simple geometry of a straight wire subject to pure torsion is amply sufficient to represent the stress relaxation of a helical spring. In the next section the creep hardening/softening of the material is examined in this context.
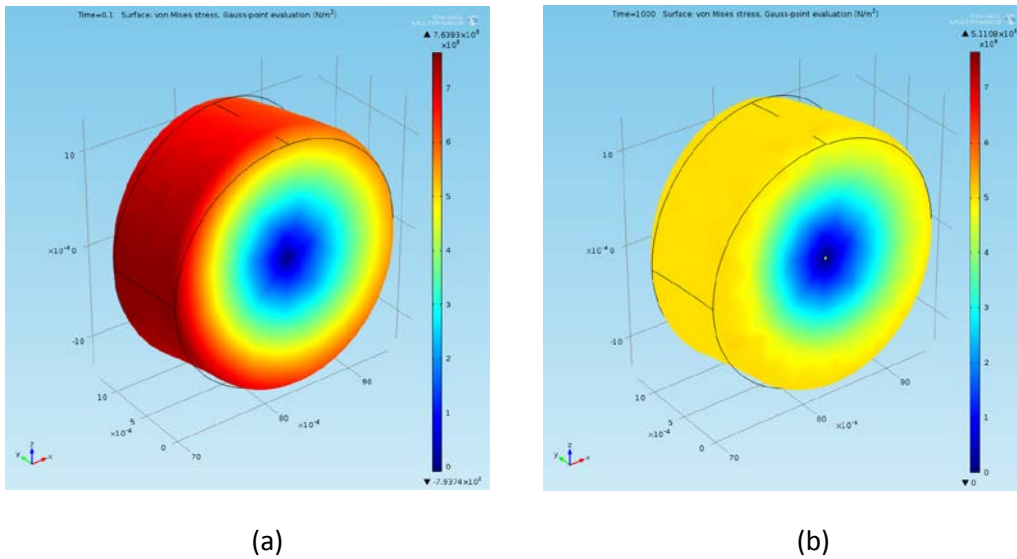

| (a) | (b) |

Figure 7 : Finite element calculations for the stress relaxation at 600°C at δ=10mm for a 7.2^{o} section of the helical spring at (a) before relaxation and (b) after 1000 seconds. The slightly asymmetric

stress state is due to the curvature of the spring wire, with the larger stresses on the inside of the wire.

3.5 Effect of back stress and tertiary creep on stress relaxation

In this section, the time-dependence of the material creep parameters $A(t)$ and $\alpha(t)$ is considered. Including dislocation multiplication using **(3.14)** is typically very important for nickel-based superalloys which demonstrate only a small amount of primary creep (up to strains of 0.2-0.3%), rapidly switching to a distinctive tertiary creep regime with an exponential strain rate without a significant secondary creep regime. Equation **(3.14)** is readily integrated with respect to time to give

$$\rho(t) = \rho_0 \left(1 + \frac{1}{\sqrt{3}} K_0 \gamma^c(t)\right). \tag{3.24}$$

Under the most extreme circumstances of a maximum shear strain of 0.68%, this suggests a maximum dislocation density of $2.2\rho_0$. Whilst this is not insignificant, it is only at a small region of the wire cross-section, and hence in general tertiary creep is not expected to be of great importance in this application. This is demonstrated in Figure 8 where the difference between the model with back stress and the model with back stress and tertiary creep is small.

A back stress is generated due to transfer of the load from the matrix to the particles as creep of the matrix progresses. If the applied load $\tau = \tau_0$ is constant then **(3.13)** predicts that

$$H(t) = H^* \left(1 - \exp\left(-(1+b)\frac{G\gamma^c}{\tau_0}\right)\right) \tag{3.25}$$

where $b = \frac{(1+v)(1+2f)}{3(1-f)} - 1$ is a constant. This describes a monotonic progression from zero to the maximum value of H^* (which is always between 0 and 1). However, for the particular case of stress relaxation considered here, the applied load is not a constant and hence **(3.13)** can be expressed as

$$\frac{dH}{dt}\tau + H\frac{d\tau}{dt} = \frac{Ef}{3(1-f)}\left(1 - \frac{H}{H^*}\right)\frac{d\gamma^c}{dt}. \tag{3.26}$$

Given $\tau = G(gr\phi - \gamma^c)$ this becomes

$$\left[\frac{Ef}{3(1-f)}\left(1 - \frac{H}{H^*}\right) + HG\right]^{-1}\frac{dH}{dt} = \frac{1}{G(gr\phi - \gamma^c)}\frac{d\gamma^c}{dt} \tag{3.27}$$

which can be integrated over time to give

$$H(t) = \frac{a}{b}\left(1 - \left(1 - \frac{\gamma^c(t)}{gr\phi}\right)^b\right) \tag{3.28}$$

where $E = 2(1+v)G$ and $a = \frac{2(1+v)f}{3(1-f)}$. The two contributions to b arise from the rate of increase in the back stress and the rate of decrease in the applied load (due to stress relaxation). The behaviour of **(3.28)** is interesting as b can be either negative or positive. To investigate the long time predictions of the model we let $H_0 = \lim_{t\to\infty} H(t)$. For a large volume fraction ($f > 0.3$) one has

15

$b > 0$ for which $H(t)$ monotonically increases from zero to $H_0 = \min(\frac{a}{b}, 1)$. For materials in the temperature range considered in this paper one has a smaller volume fraction ($f < 0.3$) for which $b < 0$. In this case the back stress continues to develop until the maximum value $H_0 = 1$ is reached, at which point the creep process prematurely stops. The total creep strain at this point is $\gamma^c = (1 - e)gr\phi$, where $e = \left(1 - \frac{b}{a}\right)^{\frac{1}{b}}$. The final residual force in the spring once creep has stopped is therefore eP_0. The value of e only varies slightly in the context of the materials and test conditions considered here. It has a minimum value of 5% for the low gamma-prime alloy Nimonic 90 at 700°C and a maximum value of 7% for the higher gamma-prime alloy René 41 at 600°C. The associated evolution of the hardness parameter **(3.28)** is illustrated in Figure 8. Note that this is purely a stress relaxation phenomenon.

Equation **(3.16)** is solved numerically with $A(t)$ defined by **(3.9)** and **(3.24)** and $\alpha(t)$ defined by **(3.10)** and **(3.28)**. The relative effects of including the different physical processes in the model are illustrated in Figure 8. It can be seen that inclusion of the back stress slows the predicted stress relaxation rate, typically by a factor of about two. As predicted from **(3.28)**, the hardness parameter H converges to unity for the case of stress relaxation with $b<0$. This results in a cessation of the relaxation, with a finite residual force remaining in the spring. As described previously, consideration of the tertiary creep process due to dislocation multiplication **(3.24)** slightly accelerates the stress relaxation process towards its end but is generally of little significance. These two effects are clearly not significant enough to explain the very large discrepancy between the stress relaxation predictions for the experimental spring data (fit) and those from the extruded sample data (uniaxial) in Figure 6. The effects of microstructural features such as the gamma-prime volume fraction and particle size are now investigated in the next section.
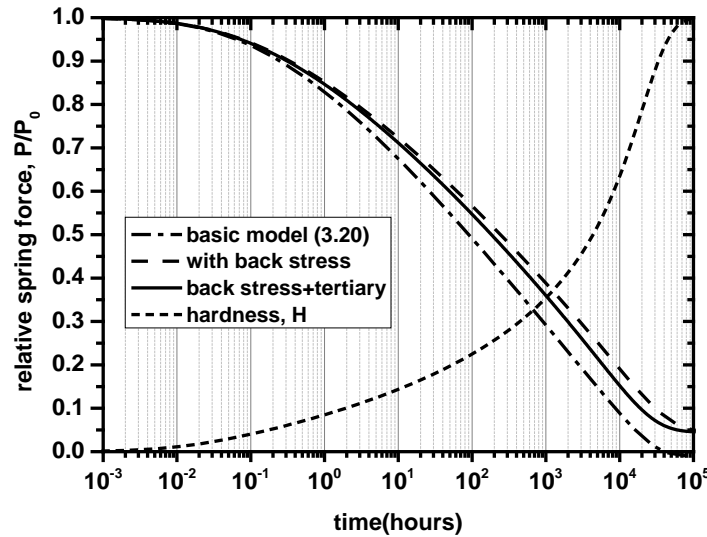

Figure 8: The contribution of back stress and tertiary creep to stress relaxation of the spring. The evolution of the hardness parameter H is also shown. As H approaches unity the relaxation of the spring force stops at 5% of the initial value.

3.6 Predicted influence of coarsening and further precipitation on stress relaxation

The $sinh$ term in the creep law **(3.10)** is very sensitive to the value of α. Therefore it is of some interest to determine the sensitivity of the stress relaxation of a spring to various parameters that affect this term. Firstly, Dyson [13] proposes that particle coarsening occurs due to classic Ostwald ripening according to the following expression

$$r_p^3(t) = r_p^3(0)\left[1 + 3x10^6 \exp\left(-\frac{3x10^5}{RT}\right) t\right] \tag{3.29}$$

At 600°C this predicts that an increase in radius of 10% will take over 3000 years and even at 750°C it is expected to take over 7 years, so it seems reasonable to neglect this.

The other contribution from the precipitate-hardening particles is their volume fraction. Previously it has been assumed that this is a constant, $f(T)$, determined from the operating temperature T using **(3.11)**. However, the volume fraction at the start of the test is that in the as-received state. This depends on the previous heat treatment of the sample. Here it is assumed that the volume fraction of gamma-prime particles in the as-received state is the equilibrium value at the final heat treatment temperature, T_{HT}, given in Table 2. The change in the volume fraction over time can be described by the Johnson-Avrami-Mehl equation [14]. Assuming that the growth is nucleation-controlled and that new precipitates rapidly grow to the same size as the existing precipitates, r_p, then the growth exponent is 1. In this case the volume fraction of particles evolves as

$$\frac{df}{dt} = \mu(f(T) - f) \tag{3.30}$$

subject to $f(0) = f(T_{HT})$, where the constant μ is related to the nucleation rate (and hence is a function of temperature). Precipitation of gamma-prime in the temperature range under consideration is usually quite rapid, typically occurring over the first 1-10 hours.

It is commonly assumed in alloys that they will precipitation harden during service, but in this case the creep is so rapid that significant deformation can take place before precipitation hardening occurs. The influence of the initial gamma-prime volume fraction on the early stages of stress relaxation in a Nimonic 90 spring at 600°C is illustrated in Figure 9 for μ=0.1 per hour. The lower curve in Figure 9a shows the change in f for T_{HT}=900°C, from its initial low value of 11% (during which significant stress relaxation occurs) up to its final value of 24% (as which point the stress relaxation slows). It is clear that a large difference between the age-hardening temperature and the in-service temperature of the alloy can have a huge effect on the early stages of the stress relaxation. It is expected that this effect will have the most influence on the behaviour of the René 41 springs, as they have the highest final age-hardening temperature of 760°C, as shown in Table 2. Figure 9b shows how this can also affect the evolution of the back stress in the springs.
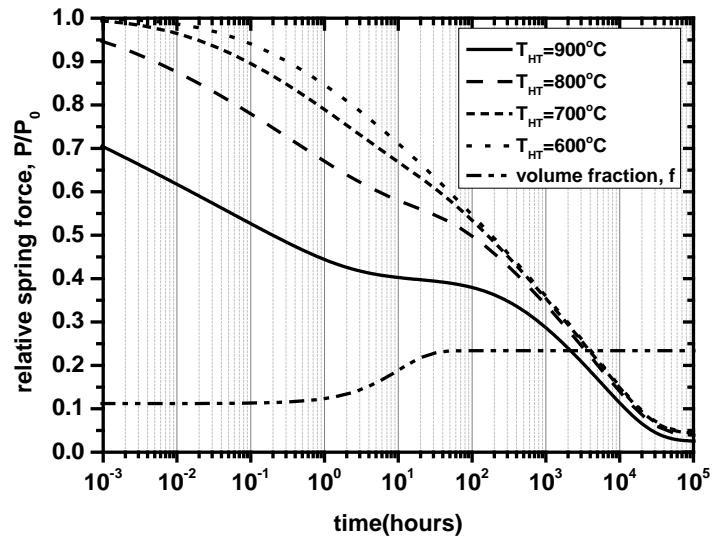
(a)
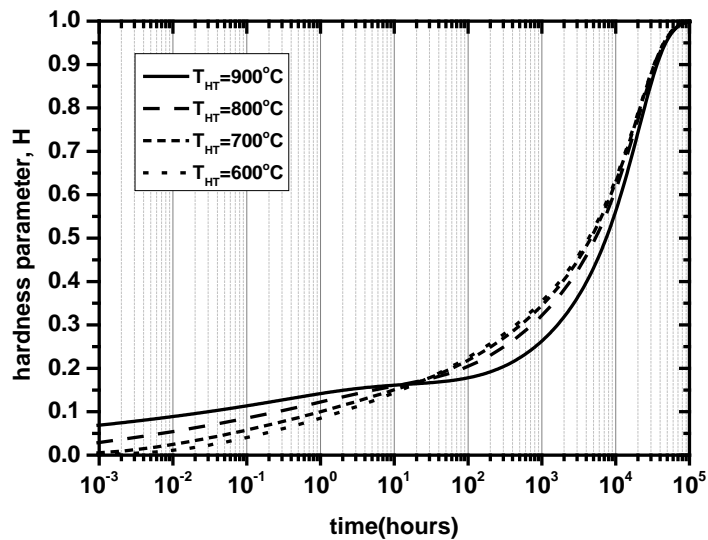
(b)

Figure 9 : The effect of further gamma-prime precipitation on the stress relaxation of a Nimonic 90 spring at 600°C (a) stress relaxation and gamma-prime volume fraction, (b) harness parameter H.

3.7 Modelling summary

The stresses on the outside of the spring wire have been shown to be very large, within the vicinity of the yield strength of the material in the stipulated temperature range. A basic stress relaxation model for a cylindrical wire under pure torsion based on a variant of the Dyson creep model has been derived in **(3.21)**. This has been shown to predict a linear regime **(3.23)** in a plot of relative spring force $P(t)/P(0)$ against $\log_{10}(t)$. In Figure 7, it has been shown that this simple model is a

good approximation for the stress relaxation of a helical spring, although the creep rate must be adjusted to be significantly larger than that observed in uniaxial extruded creep specimens. Solving the full equation **(3.16)** numerically allows for the development of a back stress **(3.28)** and the distinctive tertiary creep of nickel-based superalloys **(3.27)**. Figure 8 demonstrates that inclusion of the back stress can result in a decrease in the creep rate, although well within the range of uncertainty for the creep model. It does, however, result in the spring force relaxing to a finite non-zero value of roughly 5-7% of the initial value. As expected, tertiary creep is of little consequence as the strains here are well below 1%. As creep is rapid, particle coarsening **(3.29)** is negligible. One significant factor that is not included in the basic model **(3.21)** is the effect of further precipitation in the first 1-10 hours of service if the material is functioning well below the heat treatment temperature, as illustrated in Figure 9a. The predictions of the full model **(3.16)** are now compared with the experimental results in the following section.

4. Discussion

The predictions of the model developed in section 3 are compared with experimental data in section 4.1. The sensitivity of the test specimens to stress is found to be much less than one would expect from the stress relaxation model. This is explored in section 4.2. The consequence of this is to look at other factors that could induce this type of response. Section 4.3 considers the effect of residual stresses in the springs to offer an explanation for this phenomenon.

4.1 Comparison with experimental results

The predicted stress relaxation responses for the three materials introduced in section 2, Nimonic 90, Haynes 282 and René 41, are shown for different temperatures as the dashed lines in Figures 10, 11 and 12 respectively for the case of δ=10mm. In every case, the measured relative spring force decays much faster than the uniaxial creep test data predicts. In the extreme case of Nimonic 90 at 700°C in Figure 10c, the stress relaxation in the springs is three orders of magnitude faster than expected in a uniaxial tensile creep test specimen. This suggests that one or more of the material parameters in the spring wire are substantially different to those in the uniaxial test specimens.

The parameters that most depend on the particular processing conditions are the radius of the gamma-prime particles, r_p, and the initial dislocation density, ρ_0. As r_p appears inside the $sinh$ term, a small change in its value can have a very significant effect. By increasing α, it can dramatically increase the stress-dependence and temperature-dependence of the stress relaxation rate. This is commensurate with the observations for Nimonic 90, where the rapid stress relaxation at 700°C is not picked up by the model with r_p=10nm. It is therefore tempting to increase the radius. The other consequence of increasing r_p however is that it further accentuates the difference between the δ=6, 8 and 10mm curves. Overall the model substantially overestimates the variation in the spring force relaxation curves for the different applied displacements. This strong δ-dependence is to be expected for the creep of most metals, as they generally have a highly non-linear stress-dependence. However, all the experimental measurements showing reduced δ-dependence, particularly Nimonic 90 at 700°C and René 41 at 650°C and 700°C. For this reason, the value of the gamma-prime radius r_p is assumed to remain unchanged, with the initial dislocation density ρ_0 as the fitting parameter.

The different parameters used are compared in Table 4. This shows that the spring relaxation model is a factor of 5 (Haynes 282), 20 (René 41) and 67 (Nimonic 90) times faster than expected from the uniaxial tensile creep test data. A potential explanation for this substantial difference is the different processing conditions of the spring versus the extruded uniaxial test sample. Once extruded into spring wire, the alloys are then wound into a helical coil of radius R. This bending induces a strain gradient of $1/R$. Torsional investigations of strain gradient plasticity theory [19,25-28] suggest that there must be an associated density of geometrically necessary dislocations of $1/Rb=50\times10^{10}$ m^{-2} to accommodate this deformation, where b=0.25nm is the Burgers vector. There is also a strain gradient of $\phi_c = h/LR$ due to the twisting of the wire upon coiling, where h and L are the height and wire length of the resulting spring. This has an associated dislocation density of ϕ_c/b=5x10^{10} m^{-2}. The predicted total dislocation density due to the formation of the spring is therefore 55x10^{10} m^{-2}. This is clearly much higher than the values anticipated from the calibration of the uniaxial creep model in Table 4. A proportion of these dislocations will annihilate upon the post-forming heat treatment, although as these are geometrically necessary dislocations, required to accommodate the plastic strain, they are typically all of the same orientation. This makes them more resistant to annealing, as whilst statistically stored dislocations exist in populations of equally distributed orientations, geometrically necessary dislocations are all of a similar orientation and hence unable to annihilate each other by combination.

As indicated in Table 2, the creep responses and microstructures of the three alloys are only expected to be marginally different prior to the coiling process, or in fact after the coiling process. The main difference between them is expected to be after the subsequent post-coiling heat treatment. It is telling that the alloy that provides the best performance, closest to its uniaxial creep test benchmark, is Haynes 282, which has a two-stage precipitation heat treatment. The two stage process provides greater control of the precipitating species, particularly carbides and the gamma-prime phase. The next closest alloy is René 41 which has a heat treatment nearly 200°C higher than the poorest performing alloy, Nimonic 90. The resistance to creep of René 41 is initially very poor, with a large reduction in the spring force in the first 10 hours. The model fits the data closely, and demonstrates that this early drop can be explained by the low gamma-prime fraction that exists in the alloy at the commencement of the test due to the large difference between the heat treatment temperature (f= 18% at T_{HT} =899°C) and the test temperatures (f= 27% at T =650°C and f= 29% at T =700°C). The subsequent hardening of the alloy is consistent with further precipitation of gamma-prime at the lower operating temperatures. So a large difference in the dislocation density between the extruded section (used for uniaxial creep data) and the coiled wire (used in springs) would appear to be a valid explanation for the reduction in creep-resistance of the spring materials. Confirmation of this will be the subject of further microstructural investigation. One outstanding unexplained feature, however, is the lack of variation in the experimental data for the different loading cases of δ=6, 8 and 10mm. The model shows a large separation between the three (upper, middle and lower) curves for these loading cases, which is not reflected in the experimental data. Reasons for this discrepancy are investigated in the next section.

Alloy	Uniaxial creep test fit	Stress relaxation spring fit	Factor increase
Nimonic 90	0.3x10^{10} m^{-2}	20x10^{10} m^{-2}	67
René 41	10^{10} m^{-2}	20x10^{10} m^{-2}	20

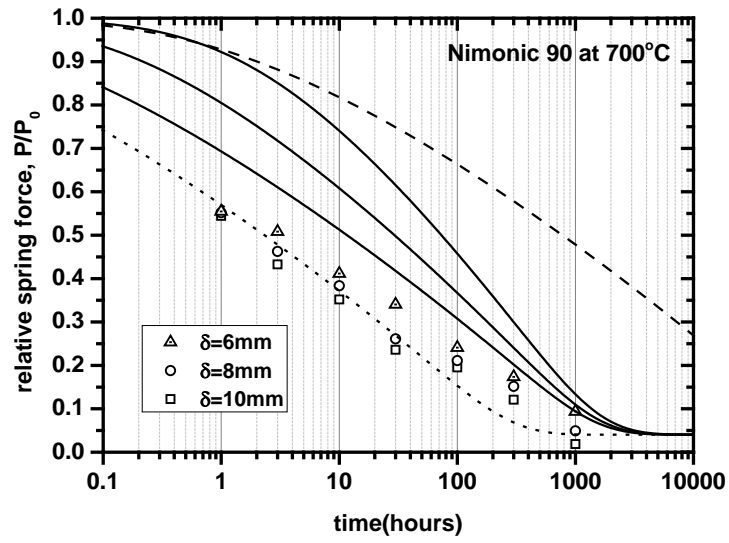| Haynes 282	10^{10} m^{-2}	5×10^{10} m^{-2}	5

Table 4 : Comparison of the values of the initial dislocation density ρ_0 used to fit the creep data from uniaxial tensile tests in Figure 5 and the values used to fit the spring force relaxation tests in Figures 10, 11 and 12.
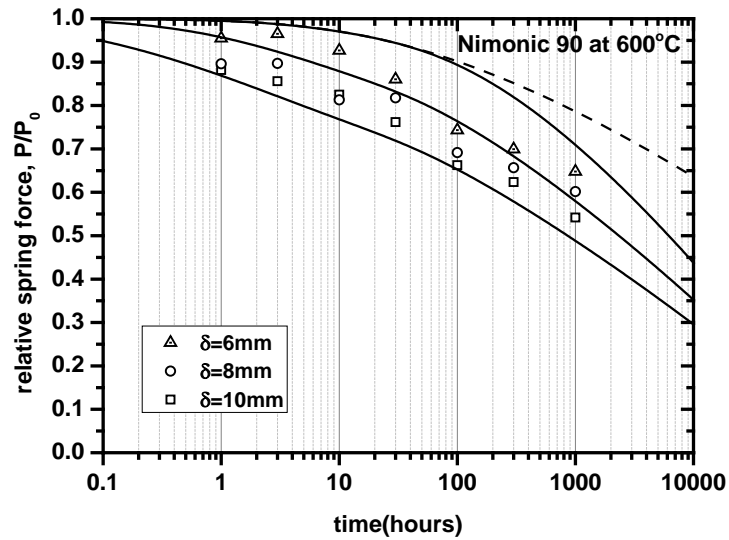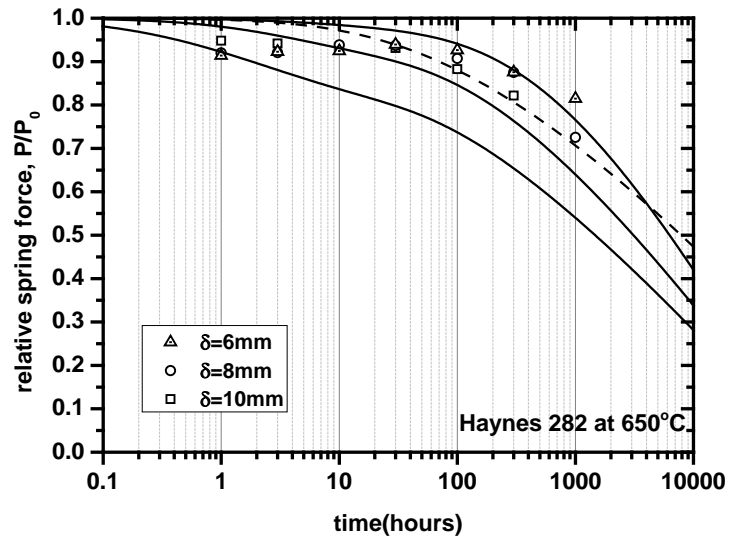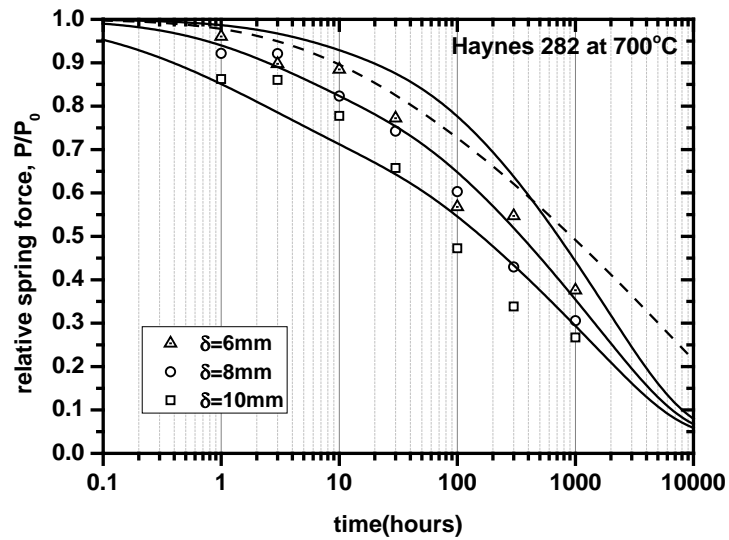

(a)
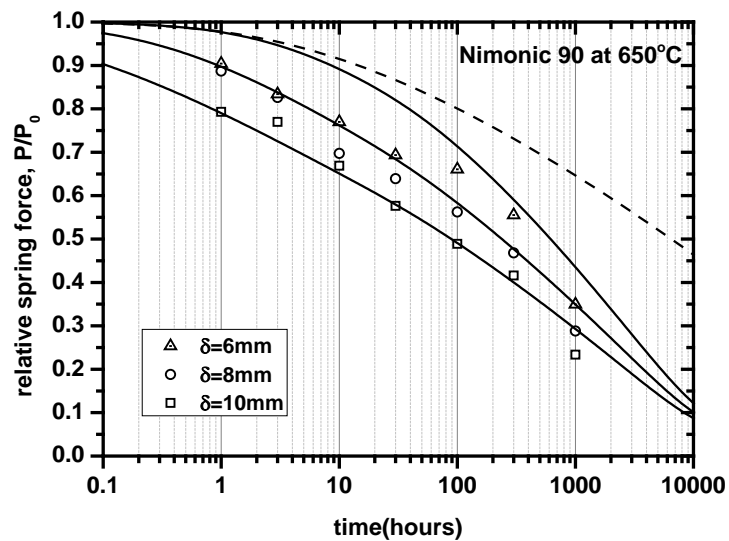
(b)

(c)

Figure 10 : Comparison between the stress relaxation model and the experimental data for Nimonic 90 at (a) 600°C, (b) 650°C and (c) 700°C. The solid lines are the predictions for δ=6mm (top), 8mm (middle) and 10mm (lower). The dashed line is the prediction for δ=10mm using the model data fitted to the uniaxial creep model shown in Figure 5. In (c) the dotted line is the prediction for $\rho_0 = 10^{12} \, m^{-2}$.
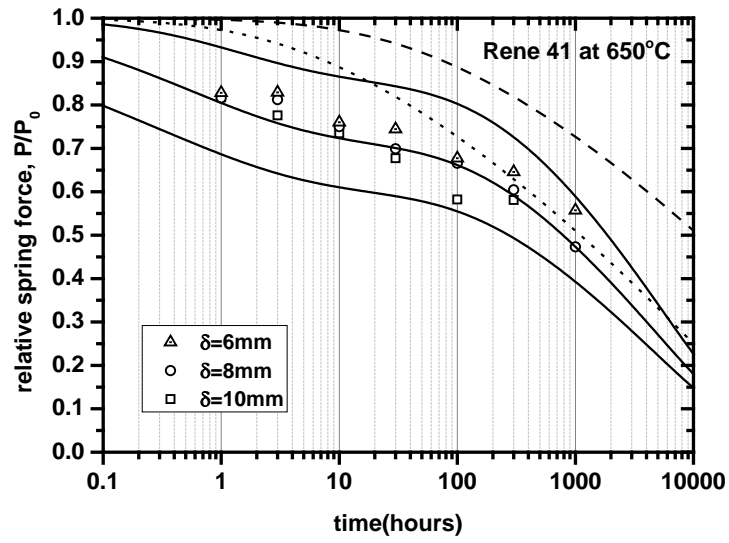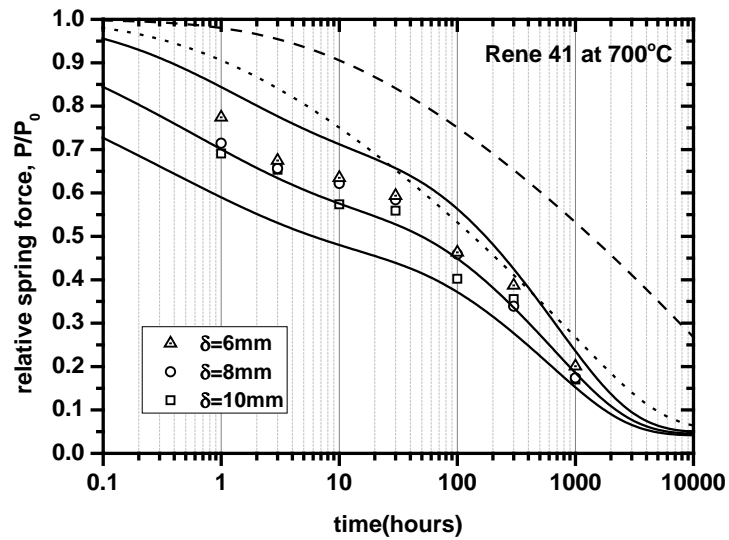
(a)

(b)

Figure 11 : Comparison between the stress relaxation model and the experimental data for Haynes 282 at (a) 650°C, and (b) 700°C. The solid lines are the predictions for δ=6mm (top), 8mm (middle) and 10mm (lower). The dashed line is the prediction using the model data fitted to the uniaxial creep model for δ=10mm.

(a)

(b)

Figure 12 : Comparison between the stress relaxation model and the experimental data for René 41 at (a) 650°C, and (b) 700°C. The solid lines are the predictions for δ=6mm (top), 8mm (middle) and 10mm (lower). The dashed line is the prediction using the model data fitted to the uniaxial creep model for δ=10mm.

4.2 Investigation of the apparent low sensitivity of the springs to stress

The unexpectedly low stress-dependence in the experimental data is investigated through the predictions of a simple power law creep model

$$\frac{d\gamma_c}{dt} = B\left(\frac{r\phi - \gamma_c}{\gamma_0}\right)^n \tag{4.1}$$

where B and γ_0 are temperature-dependent material parameters, and the stress exponent, $n > 1$, can be varied to see the influence of the magnitude of the non-linearity on the stress relaxation response. Integrating (4.1) with respect to time and inserting the result in **(3.20)** defines the relative spring force evolution for power law creep to be

$$\frac{P(t)}{P_0} = {}_2F_1\left(\left[\frac{1}{m}, \frac{4}{m}\right], \left[1 + \frac{4}{m}\right], -m\left(\frac{a\phi}{\gamma_0}\right)^m \left(\frac{B}{\gamma_0}\right)t\right) \tag{4.2}$$

where ${}_2F_1([i,j],[k],x)$ is the hypergeometric function, and $m = n - 1$ is assumed to be a positive integer. For the linear case (n=1) this reduces to $\frac{P(t)}{P_o} = \exp(-B\gamma_0^{-1}t)$.

The effect of the stress exponent on the shape of the spring force relaxation curve is shown in Figure 13a. The value of the relevant material constant $B\gamma_0^{-n}$ is chosen so that the curves coincide at P/P_0=0.7 at a similar time. The exponent that best fits the material data shown is n=8. This has a relatively shallow rate of decay, with the steepness of the curves increasing as the exponent decreases. With a low stress exponent, the high stresses on the outside of the wire are only marginally more important than the lower stresses near the centre, and hence, once initiated, the creep process continues quite rapidly. In the case of the higher stress exponents, the high stresses on the surface of the wire dominate the creep process initially, but are rapidly reduced. The consequence of this is a fairly rapid relaxation of the spring force early on, followed by a slower relaxation as the resulting lower elastic stresses in the wire provide a significantly lower driving force for the creep process. The conclusion from Figure 13a therefore is that the observed spring relaxation force data is consistent with a highly stress-sensitive creep model, such as a high exponent (n=8-10) power law creep law or the $sinh$-dependence of the Dyson creep model **(3.16)**. The linearity of the uniaxial creep test data in Figure 5 clearly demonstrates an exponential Dyson-type dependence, and in fact would, if anything, appear to underestimate the stress-sensitivity for the higher creep strain data at 0.5%. This conclusion is in contrast to the picture presented in Figure 13b however. This illustrates how the relaxation profiles are expected to vary with the applied displacement δ for a test at a particular temperature. It is clear that a strong dependence on δ is observed for a high stress-sensitivity (n=8) as expected, and that the strength of this dependence reduces with decreasing n until the profile becomes essentially stress-independent for the linear case (n=1) where there is just a single master curve for all δ. Comparison with the experimental data shows that the observed variation between the δ=6,8 and 10 mm curves is more compatible with a less stress-sensitive model (n=2-4), with the extreme case of the data for René 41 in Figure 12 demonstrating a variation more compatible with n=1-2, although the curves are the wrong shape.

We have established that a high stress-dependence is expected from the uniaxial creep data and is consistent with the shapes of the profiles, if not the variance. Is there then a difference between the creep process in uniaxial tension and the creep process in torsion? This seems unlikely as rigorous

experiments on Nimonic 80A in a similar stress and temperature range showed no significant difference between the tensile and torsional creep tests for the range of strains that apply here of less than 1% [18]. This finding is also supported by torsional creep tests on other materials [23,24].

Another explanation is the difference between creep and stress relaxation, although again, in experimental tests there is no substantial observed difference between the two processes, especially in terms of the stress exponent n [21]. A change in the creep mechanism is another factor to be considered. At very high stresses, particle shearing and even possibly initial yielding could be expected to dominate above 600MPa or so [4]. However, there is no evidence for the action of these processes as these would further differentiate between the low stress and high stress tests, particularly at the start, and this is not the case. Only a very small region on the surface of the δ=10mm test sample spring is likely to experience such high stresses. At lower stresses, typically less than 100MPa [4], diffusion creep is expected to be the operating process. This mechanism is associated with a low stress exponent of n=1-2. This would be expected to induce a slightly enhanced creep rate in low stress regions, leading to a more rapid relaxation near the end of the springs creep life with a smaller stress-variance. This would manifest as a transition from the high exponent profile (n=8) to the lower exponent profile (n=1-5) at the latter stages of relaxation, but it would not affect the profile when higher stresses dominate in the early stages. The remaining explanation is the possibility of significant residual stresses existing in the spring. This final consideration is explored in the next section.
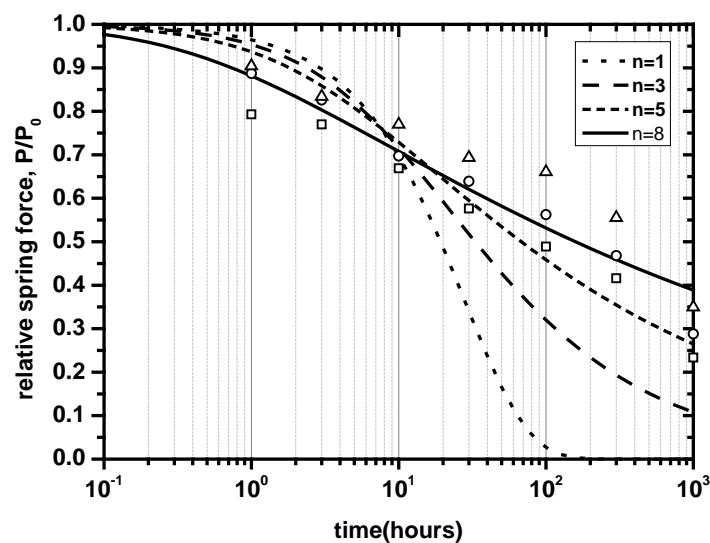
(a)
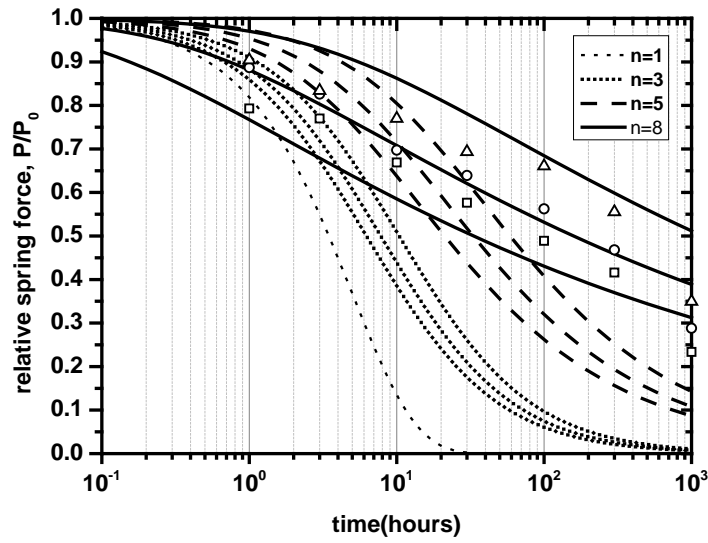
(b)

Figure 13: The dependence of (a) the slope, and (b) the variance, of the relative spring force evolution on the stress exponent n , shown against the experimental data for Nimonic 90 at 650°C for (a) δ=8mmm and (b) δ=6 (upper), 8 (middle) and 10mm (lower).

4.3 Residual stresses

If the springs already have an internal stress state then the effects of a superimposed stress state due to loading can have a reduced (or possibly increased) effect. As discussed in section 4.1, it is normally expected that any residual stress will be removed by the heat treatment, although this is typically applied to cases where the residual stress arises from statistically stored dislocations which are more readily annihilated than geometrically necessary dislocations as they have an equal population of positive and negative Burgers vectors. Therefore the existence of a residual stress state is compatible with the explanation that a remnant population of dislocations strongly enhances the stress relaxation rate of coiled wire. It is therefore also expected that the residual stresses in Haynes 282 will be lower than in the other two alloys, as this experiences a two stage precipitation heat treatment. It is telling therefore that the relaxation profiles for Haynes 282 in Figure 11a and 11b demonstrate a larger δ-dependence than the other two alloys at similar temperatures, in agreement with the theoretical predictions.

Residual stresses will arise due to the bending and twisting of the wire into a helix, and both can interact with the relaxation of the torsional stresses through the effective stress according to **(3.12)**. As the exact post-heat treatment residual stress state is not known, a simple model is proposed here. Firstly, only the residual stresses due to twisting are considered as these are superimposed on the existing torsional shear stress state. It is also assumed that the forming operation will cause the torsional shear stresses to exceed yield across the entire wire cross-section, such that the shear strain $\gamma(r) = \gamma_Y$ is constant, where $\tau_Y = G\gamma_Y$ is the shear yield stress. Upon elastic unloading there is elastic recovery via a rotation per unit length of ϕ_R. The net torque in the cross-section,

27

$Q = 2\pi G \int_0^a (\gamma_Y - r\phi_R)rdr$, must be zero. Therefore $\phi_R = \frac{4\gamma_Y}{3a}$ and the residual torsional stress state is represented by the strain field $\gamma_R(r) = \gamma_Y \left(1 - \frac{4r}{3a}\right)$. This is positive in the centre of the wire and negative near the surface of the wire. As this has no net torque, it has no effect on the force-displacement relationship for the spring. This stress field is also compatible with the observation that the springs do not yield under high compressive loads when the stresses at the surface are expected to be of sufficient magnitude for this to occur. The residual stresses therefore only appear in the creep rate, such that **(3.17)** becomes

$$\frac{d\gamma^c}{dt} = \frac{1}{2}A_0 \left[\exp(\beta(\gamma_R(r) + r\phi - \gamma^c)) - 1\right]. \tag{4.3}$$

The analytical solution for the basic creep model **(3.20)** is therefore

$$\frac{P(t)}{P_0} = -\frac{4}{\beta\phi a^4} \int_0^a r^2 \ln\left[1 - e^{-\frac{1}{2}A_0\beta t}\left(1 - e^{-\beta(\gamma_R(r) + r\phi)}\right)\right] dr. \tag{4.4}$$

For the proposed linear residual strain field this has an analytical solution, similar to **(3.21)**, although it is too unwieldy to reproduce here. To estimate the yield strain we assume $\gamma_Y \approx \sqrt{3}\frac{\sigma_{UTS}}{E}$. As the strain is very large it is reasonable to assume that the stresses approach the UTS of 1175MPa. The modulus is about 209GPa for Nimonic 90 giving a rough value of γ_Y=1%. This is a large value, and is therefore expected to have a significant effect. In reality it is unlikely that such a high residual strain exists after heat-treatment, but taking into account the additional interaction with the residual strains due to bending (approximately 10 times larger) that are of a similar form, this may not be unreasonable. Figure 14 compares the results for Haynes 282 at 700°C with a residual torsional stress state and without any residual stress (as in Figure 11b). It is clear that the inclusion of a residual stress field can significantly reduce the δ-dependence of the stress relaxation profile with a relatively small change in the shape of the curve. In the example in Figure 14, the residual strain model now demonstrates a variance which is smaller than the experimental data. This fits with the prediction that the Haynes 282 springs are unlikely to contain substantial residual stresses due to their high temperature two stage heat treatment. The observed variance is, however, much closer to that observed in experiment for Nimonic 90 in Figure 10 and René 41 in Figure 12.
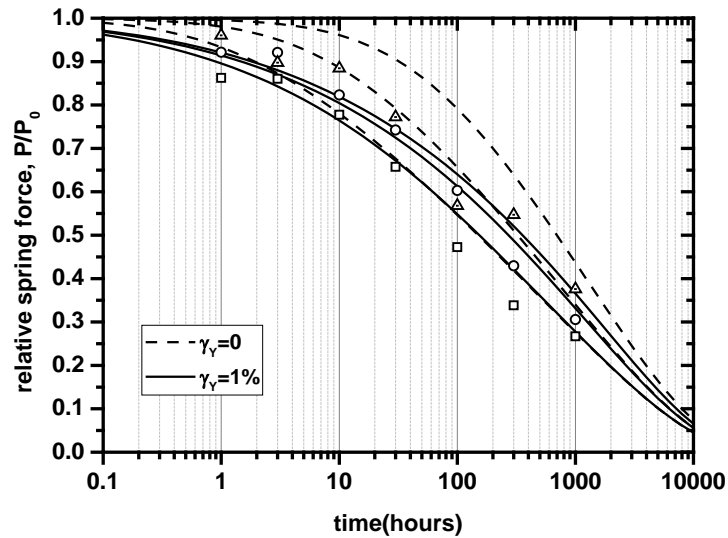
Figure 14 : Effect of a residual torsional stress ($\gamma_Y = 1\%$) on the relaxation of the spring force compared to the predictions without a residual stress ($\gamma_Y = 0\%$) from Figure 11b. The variance between the δ=6mm (upper), 8mm and 10mm (lower) curves is greatly reduced for a yield strain of γ_Y=1%.

5. Summary

The stress relaxation of three nickel-based superalloy springs has been investigated at temperatures between 600°C and 700°C. Experimental results indicate that the springs relax very quickly, typically degrading to 50% of their initial spring force within 1-1000 hours. The best performing material is Haynes 282, followed by René 41 and then Nimonic 90. The stresses near the surface of the spring wire are calculated to be approaching the yield stress of the alloy (if residual stresses are neglected). A model based on the torsional creep of a cylindrical wire using a modified version of the Dyson creep model has been used to predict the stress relaxation response of the springs. It is found that the expected performance of the materials is between one and three orders of magnitude higher than the observed response. The origin of this poor performance of nickel-based superalloys in spring applications is explored within the context of the model. Coarsening of the precipitate-strengthening gamma-prime phase is found to be a negligible effect, as is the evolution of damage, the transfer of stress from the matrix to the particles, and the increase in the dislocation density with strain. The remaining phenomena that are expected to significantly enhance the stress relaxation of the materials are: the high density of geometrically necessary dislocations in the spring material due to the bending and torsion induced in a coiled spring wire during the manufacturing process, the resistance of these dislocation populations to heat treatments, the resulting persistent residual stresses derived from these dislocations, and the inability of these materials to effectively precipitation harden during service due to the very rapid initial stress relaxation rate.

Acknowledgements

References

1. "Measurement of creep at high temperatures using helical springs", Boardman, F.D., Ellen, F.P., and Williamson, J.P., The Journal of Strain Analysis for Engineering Design, 1 140 (1966).
2. "On the analysis of creep tests using helical spring specimens", Lewthwaite, G.W. and Smith, R.T., Brit. J. Appl. Phys. 18 1012-1016 (1967).
3. "The use of helically coiled springs in creep experiments with special reference to the case of Bingham flow", Crossland, I.G., Jones, R.B. and Lewthwaite, G.W., J. Phys. D: Appl. Phys., 6, 1040 (1973).
4. "Comparison of physical and empirical deformation maps for Nimonic 90", Harrison, G.F., Evans, W.J, and Winstone, M.R. , Mater Sci Technol, 25, 249-257 (2009).
5. "Microstructure based creep constitutive model for precipitation strengthened alloys", Dyson, B.F., Mater Sci Technol, 25, 213 (2009).
6. "FEM for springs" Editors : Shimoseki, M., Hamano, T., Imaizumi, T., Springer-Verlag (ISBN 3-540-00046-1)
7. "Materials for springs" Editor : Yamada, Y, Springer-Verlag (ISBN 978-3-540-73811-4)
8. "Simplified Stress Calculation Method for Helical Spring", Watanabe, K., Hamamoto, H., Ito, Y. and Isobe, H., Proceedings of Advanced Spring Technology, Japanese Society of Spring Engineers 60th Anniversary International Symposium, Nagoya, Japan (2007).
9. "Modelling creep of nickel alloys in high temperature power plant", Atkinson, H.V., and Gill, S.P.A., Chapter 21, Structural alloys for power plants, Woodhead publishing (2012).
10. "Multiscale microstructure modelling for nickel based superalloys", Basoalto H.C., Brooks J.W. and Di Martino I. Mater Sci Technol, 25, 221-227 (2009).
11. "A novel finite element method for helical springs", Jiang, W.G. and Henshall, J.A., Finite Elements in Analysis and Design 35 363-377 (2000).
12. "CDM predictions of creep damage initiation and growth in ferritic steel weldments in a medium-bore branched pipe under constant pressure at 590°C using a four-material weld model", Mustata R., Hayhurst R. J., Hayhurst D. R. and Vakili-Tahami F. , Arch Appl Mech, 75, 475-495 (2006).
13. "Use of CDM in Materials Modeling and Component Creep Life Prediction", Dyson, B.F., J Pressure Vessel Technol, 122, 281-296 (2000).
14. "Modelling of materials properties in duplex stainless steels', Li, X., Miodownik, A. P. and Saunders, N., Mater Sci Technol, 18, 861-868 (2002).
15. "Nimonic alloy 90" datasheet, Special Metals.
16. "René alloy 41" datasheet, Special Metals.
17. "Haynes 282" datasheet, Haynes International.
18. "Creep of nimonic 80A in torsion and tension", Dyson BF, McLean D, Metal Science 11:37–45 (1977).
19. "Strain gradient plasticity: Theory and experiment", Fleck, N.A., Muller, G.M., Ashby, M.F. and Hutchinson, J.W., Acta Metal. Mater. 42 475 (1994).

20. "Creep modelling in helical springs at 600°C", Anumula, V.S.K., Internal report, University of Leicester,UK (2012).

21. "Prediction of creep properties for two nickel-base superalloys from stress relaxation testing", Beddoes, J. The Journal of Strain Analysis for Engineering Design 46, 416 (2011).

22. "The Nimonic Alloys", W Betteridge, Edward Arnold (Publishers) Ltd, London, 222-225 (1959).

23. "Creep-Behavior Of Copper Under Plane-Stress State", Z. Kowalewski, Int J Plasticity, 7, 387-404 (1991).

24. "Relaxation Behavior And Modeling ", E. Krempl, Int J Plasticity , 17, 1419-1436 (2001).

25. "Toward A Further Understanding Of Size Effects In The Torsion Of Thin Metal Wires: An Experimental And Theoretical Assessment " D.B. Liu, Y.M. He, D.J. Dunstan, B. Zhang, Z.P. Gan, P. Hu, H.M. Ding, Int J Plasticity , 41, 30-52 (2013).

26. "A Dislocation Density Based Strain Gradient Model, S. Brinckmann, T. Siegmund, Y.G. Huang, Int J Plasticity, 22, 1784-1797 (2006).

27. "Elastic Limit And Strain Hardening Of Thin Wires In Torsion", D.J. Dunstan, B. Ehrler, R. Bossis, S. Joly, K.M.Y. P'ng, A.J. Bushby, Phys Rev Lett, 103, 155501 (2009).

28. "Finite Deformation Analysis Of Mechanism-Based Strain Gradient Plasticity: Torsion And Crack Tip Field", K.C. Hwang, H. Jiang, Y. Huang, H. Gao, Int J Plasticity, 19, 235-251 (2003).